



**HAL**  
open science

# Dimple influence on load carrying capacity of parallel surfaces

M.-P. Noutary, N. Biboulet, A.A. Lubrecht

► **To cite this version:**

M.-P. Noutary, N. Biboulet, A.A. Lubrecht. Dimple influence on load carrying capacity of parallel surfaces. *Tribology International*, 2020, 149, pp.105452 -. 10.1016/j.triboint.2018.10.033 . hal-03490518

**HAL Id: hal-03490518**

**<https://hal.science/hal-03490518>**

Submitted on 16 Jun 2022

**HAL** is a multi-disciplinary open access archive for the deposit and dissemination of scientific research documents, whether they are published or not. The documents may come from teaching and research institutions in France or abroad, or from public or private research centers.

L'archive ouverte pluridisciplinaire **HAL**, est destinée au dépôt et à la diffusion de documents scientifiques de niveau recherche, publiés ou non, émanant des établissements d'enseignement et de recherche français ou étrangers, des laboratoires publics ou privés.



Distributed under a Creative Commons Attribution - NonCommercial 4.0 International License

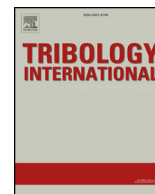


ELSEVIER

Contents lists available at ScienceDirect

Tribology International

journal homepage: [www.elsevier.com/locate/triboint](http://www.elsevier.com/locate/triboint)



## Dimple influence on load carrying capacity of parallel surfaces

M.-P. Noutary, N. Biboulet, A.A. Lubrecht\*

Université de Lyon, INSA-Lyon, LaMCoS, CNRS UMR 5259, Villeurbanne, F69621, France

### ARTICLE INFO

#### Keywords:

Piston oil control ring  
Hydrodynamic Reynolds equation  
Dimple textured parallel surfaces  
Partial texturing  
Load carrying capacity  
Multigrid

### ABSTRACT

In the case of parallel surfaces, such as the oil control ring, no load carrying capacity is generated without texture. A flow conserving multigrid code is used to solve the hydrodynamic lubrication equation described by the Reynolds equation. This code is used to investigate the influence of texture geometry (dimples) and its position along the contact. In particular the behavior of the load carrying capacity according to the texture position on the central line of the contact is studied. To generate positive load carrying capacity, only partial texturing must be used. A significant difference can be observed between inlet texturing and outlet texturing. A multigrid code has been developed that allows a comparison between Dirichlet and periodic results. A comparison with equivalent step bearings is made to analyse the load carrying capacity.

### 1. Introduction

Texturing greatly affects the performance of lubricated contacts in terms of pressure, load carrying capacity and friction. For parallel surfaces, it can generate a load carrying capacity by creating the equivalent of a Raleigh step bearing. Full texturing induces a negative load carrying capacity, but inlet texture generates a positive one. Hence the texture parameters (size, density, texture position) have to be carefully designed in order to optimize the contact performance.

Early research was conducted by Etsion, Kligerman, Halperin, Brizmer [1–6]. They performed experimental but also analytical investigations and showed the benefits of surface texturing for the enhancement of lubrication and in particular of partial texturing for parallel surfaces. In Ref. [3] for a simplified model, the distribution of the local pressure for partial texturing in the inlet and for full texturing was shown. Tonder [7] introduced the idea that performance improvement can be gained by introducing artificial roughness in the contact inlet by means of micro-structures instead of macro-structures, inducing low coefficients of friction coexisting with high hydrodynamic stiffness and damping parameters. In an experimental study, Vladescu et al. [8] analysed the influence of texturing in reciprocating contacts for various lubrication regimes. Surface texture just after reversal helps to build up the film and reduces friction. Texture pockets should entirely lie inside the contact zone. No pocket should be at the reversal point. An experimental study of Lu et al. [9] for reciprocating sliding line contacts analysed the effect of surface texturing by square dimples in various lubrication regimes. A lower friction coefficient was obtained in the boundary regime, due to the fact that the dimples act as lubricant

reservoirs. They observed that texture at the reversal point can reduce friction, this observation contradicts [8].

Many 1D analytical or numerical studies have been performed. Using a 1D model Tomanik [10] has investigated the influence of laser textured profiles for cylinder bore and rings and particularly for the oil control ring. Fowell et al. [11] explained the inlet suction phenomenon on a 1D analytical model. Fowell et al. [12] have used a 1D mass conserving numerical model to study the influence of the texture parameters according to the convergence ratio of the two main surfaces on load support and friction. Pascovci et al. [13] have performed a 1D analysis without cavitation to optimize the texture parameters for parallel sliders and made a comparison with Raleigh step bearings. Rahmani et al. [14] have used an analytical solution of the 1D Reynolds equation to optimize micro dimple texture for parallel thrust bearings.

The validity of the Reynolds model was discussed in several papers. Sahlin et al. [15] used a commercial CFD code to solve the Navier-Stokes system for a single micro-groove on one of 2 parallel surfaces. For them, fluid inertia is an important factor for the load carrying capacity and they have shown that for deep and wide grooves a vortex occurs that limits the increase in load carrying capacity. In their sequel, Menon et al. [16] also think that fluid advection is a major factor for generating load carrying capacity. In both works, cavitation was not considered. They tend to show that the Reynolds model is not adequate to study these problems. However, in Ref. [17], Dobrica and Fillon have studied the range of validity of the Reynolds equation also neglecting cavitation. They conclude that the Reynolds number and the dimple aspect ratio (dimple depth/dimple width) must be sufficiently small but nevertheless in a range that covers most useful cases.

\* Corresponding author.

E-mail address: [ton.lubrecht@insa-lyon.fr](mailto:ton.lubrecht@insa-lyon.fr) (A.A. Lubrecht).

<https://doi.org/10.1016/j.triboint.2018.10.033>

Received 27 June 2018; Received in revised form 12 October 2018; Accepted 23 October 2018  
0301-679X/ © 2018 Elsevier Ltd. All rights reserved.

Non mass-conserving models underestimate the cavitation area leading to poor estimates of the pressure as explained by Ausas et al., [18]. Ausas et al. [19] proposed a finite volume implementation of the Elrod-Adams model.

To study cavitation in dimples, Qiu and Khonsari [20] developed a mass-conservative cavitation multigrid algorithm based on the work by Vijayaraghavan and Keith [21]. Bayada, Martin and Vazquez [22] developed a mass-conserving algorithm using homogenization techniques. Using the pressure and the void fraction, Giacomoni et al. [23] built a mass-conserving complementary formulation of the 1D cavitation problem. Bertocchi et al. [24] have extended it to 2D domains and for compressible, piezoviscous and non-Newtonian fluids and used finite element methods to numerically solve the problem. An implementation of a finite volume method derived from the  $p - \theta$  Elrod-Adams cavitation model [25,26] was proposed by Profito et al. [27]. Woloszynski, Podsiadlo and Stachowiak [28] have reformulated the complementary constraint on  $p$ .  $\theta = 0, p \geq 0, \theta \geq 0$  by a continuous differentiable system  $F(p, \theta) = 0$  to which Newton's method can be efficiently applied. Biboulet [29] has successfully reduced the storage requirements and improved robustness through the use of a multigrid strategy.

Using a mass-conserving algorithm, Dobrica et al. [30] have studied the influence of full and partial texturing for parallel and plane inclined sliders, verifying in particular the benefit of inlet partial texturing and the importance of the cavitation phenomenon to generate load carrying capacity in parallel or nearly parallel structures. Cupillard et al. [31,32] used the full Navier-Stokes equation with a multi-phase flow cavitation model to study the performance of a dimple textured journal bearing and analyse the pressure buildup mechanism. In Ref. [33], Tala-Ighil, Fillon and Maspeyrot have analysed various texture configurations on the performance of a journal bearing. Shen and Khonsari ([34–37]) have numerically and experimentally studied parallel textured surfaces. For macroscopic dimples, the influence of the cavitation pressure in steady state lubrication can experimentally be significantly lower than the ambient pressure. Its value can influence simulation results. In the case of macroscopic dimples, the influence of the size and shape of the dimples on the load carrying capacity was investigated. They tried to optimize the texture shape for parallel surfaces. Gherca et al. [38–40] have recently developed a mass-conserving algorithm to study the influence of surface texturing in steady-state but also transient hydrodynamic lubrication of parallel sliders.

In this paper, a multigrid flow-conserving algorithm based on Alcouffe's paper [41] and on the Elrod and Adams [25,26] model is built. It does not show full multigrid efficiency. This is probably due to the discontinuity of the Poiseuille and Couette flow which were not well accounted for when the pressure builds up again. However, the code converges sufficiently fast and is flow conserving. It can therefore be used to study and discuss dimple textured parallel surfaces, even with deep dimples.

## 2. Problem formulation and algorithm

### 2.1. Notations

The following parameters are used.

$a$	Dimple depth [m]
$d$	Distance between dimples [m]
$h$	Geometry height [m]
$h_{oil}$	Film thickness [m]
$h_0$	Clearance [m]
$p$	Pressure [Pa]
$r$	Dimple radius [m]
$p_{amb}$	Ambient pressure
$x$	Coordinate in direction of sliding [m]
$y$	Coordinate perpendicular to direction of sliding [m]

$w$	Load carrying capacity [N]
$\eta$	Fluid viscosity [Pa.s]
$\rho$	Fluid density [kg/m <sup>3</sup> ]

### 2.2. Mass complementary formulation

The hydrodynamic lubrication of the piston ring-cylinder liner contact can be described by the Reynolds equation. According to Elrod, because of cavitation and in order to have a mass conserving algorithm, the following complementary problem is solved:

$$\frac{\partial}{\partial x} \left( \frac{\rho h^3}{12\eta} \frac{\partial p}{\partial x} \right) + \frac{\partial}{\partial y} \left( \frac{\rho h^3}{12\eta} \frac{\partial p}{\partial y} \right) - u_m \frac{\partial(\rho\theta h)}{\partial x} - \frac{\partial(\rho\theta h)}{\partial t} = 0 \quad (1)$$

with

$$(p > p_{cav} \text{ and } \theta = 1) \text{ or } (p = p_{cav} \text{ and } 0 < \theta < 1) \quad (2)$$

Where  $p$  is the hydrodynamic pressure,  $h$ , the geometry,  $u_m$  the mean velocity. The lubricant density,  $\rho$  and the viscosity,  $\eta$  can be considered constant in the studied regime. Considering that  $p$  in equation (1) is the difference between the pressure and the cavitation pressure,  $p_{cav}$ ,  $p_{cav}$  is set to 0 in equation (2). This problem will be solved on a rectangle  $\Omega$ . The difference between the ambient pressure and the cavitation pressure is denoted  $p_{amb}$ . Here the generated pressures are not very high because the considered surfaces are mainly parallel. Therefore the difference between the ambient pressure and the cavitation pressure is significant. No pressure would be generated if the cavitation pressure and the ambient pressure were identical. The pressure would not be able to decrease when entering the dimple and no extra oil would flow inside the dimple. In the cavitated area the fluid becomes a mixture of liquid, vapor and gas and  $\theta\rho$  can be viewed as the lubricant density. Here we prefer to consider the variable  $h_{oil} = \theta h$ , that represents the fluid level or an equivalent of the fluid level in the whole domain  $\Omega = [-x_0, x_0] \times [-y_0, y_0]$ . Hence  $h_{oil} = h$  in the pressurized zones and lies between 0 and  $h$  elsewhere. In this paper only the stationary case is considered and therefore, we solve the following problem:

$$\frac{\partial}{\partial x} \left( \frac{h^3}{12\eta} \frac{\partial p}{\partial x} \right) + \frac{\partial}{\partial y} \left( \frac{h^3}{12\eta} \frac{\partial p}{\partial y} \right) - u_m \frac{\partial h_{oil}}{\partial x} = 0 \quad (3)$$

with

$$(p > 0 \text{ and } h_{oil} = h) \text{ or } (p = 0 \text{ and } 0 < h_{oil} < h) \quad (4a)$$

$$p = p_{amb} \text{ on } \partial\Omega \quad (4b)$$

Two kinds of boundary conditions are considered:

- Dirichlet conditions: the pressure is set to  $p_{amb}$ , the ambient pressure, on the boundaries of the domain.
- Periodic conditions: the pressure and the geometry are periodic in the  $y$ -direction that is perpendicular to the sliding direction, while the pressure is  $p_{amb}$  on the  $x$ -boundaries of the domain.

In what follows the fluid will be considered to flow between two parallel surfaces of constant gap  $h_0$ . The stationary surface will be indented by circular dimples of radius  $r$  and depth  $a$ . For a single dimple, the cross section of the two surfaces by a plane passing through the middle of the dimple is sketched in Fig. 1. The geometry  $h$  is defined as follows:

$$h(x, y) = h_0 + \phi(x, y)$$

with

$$\phi(x, y) = \frac{a}{2} \left( 1 + \cos \left( \frac{\pi}{r} \sqrt{(x - x_i)^2 + (y - y_i)^2} \right) \right)$$

if there is a dimple of depth  $a$  centered at  $(x_i, y_i)$  and if  $(x - x_i)^2 + (y - y_i)^2 \leq r^2$  and  $\phi(x, y) = 0$  otherwise.

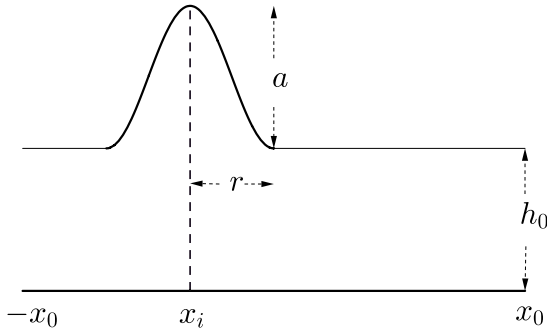


Fig. 1. Geometry: cross section through the middle of a dimple.

### 2.3. Dimensionless equations

Upper letters are used for the associated dimensionless parameters: The lengths in directions orthogonal to the surfaces are made dimensionless using  $h_0$ . In the  $x$  and  $y$  directions, a reference length  $\lambda$  is used. It could be  $\lambda = x_0$  or  $\lambda = r$ . For the pressure and the load  $p_0 = \frac{12\eta\mu_m\lambda}{h_0^2}$  and  $w_0 = p_0\lambda^2$  are respectively used.

- $A = a/h_0$  Dimensionless dimple depth
- $D = d/\lambda$  Dimensionless distance dimples
- $H = h/h_0$  Dimensionless geometry height
- $Hoil = hoil/h_0$  Dimensionless film thickness
- $P = p/p_0$  Dimensionless pressure
- $R = r/\lambda$  Dimensionless dimple radius
- $X = x/\lambda$  Dimensionless coordinate in direction of sliding
- $Y = y/\lambda$  Dimensionless coordinate perpendicular to direction of sliding
- $LCC = w/w_0$  Dimensionless load carrying capacity

With these dimensionless variables the dimensionless Reynolds equation reads:

$$\frac{\partial}{\partial X} \left( H^3 \frac{\partial P}{\partial X} \right) + \frac{\partial}{\partial Y} \left( H^3 \frac{\partial P}{\partial Y} \right) - \frac{\partial (Hoil)}{\partial X} = 0 \quad (5)$$

with the following dimensionless complementary and boundary conditions:

$$(P > 0 \text{ and } Hoil = H) \text{ or } (P = 0 \text{ and } 0 < Hoil < H) \quad (6a)$$

$$P = P_{amb} \text{ on } \partial\Omega \text{ with } \Omega = [-X_0, X_0] \times [-Y_0, Y_0] \quad (6b)$$

and

$$H(X, Y) = 1 + \Phi(X, Y)$$

with

$$\Phi(X, Y) = \frac{A}{2} \left( 1 + \cos \left( \frac{\pi}{R} \sqrt{(X - X_i)^2 + (Y - Y_i)^2} \right) \right) \quad (7)$$

if there is a dimple of depth  $A$  centered at  $(X_i, Y_i)$  and if  $(X - X_i)^2 + (Y - Y_i)^2 \leq R^2$  and  $\Phi(X, Y) = 0$  otherwise.

### 2.4. Algorithm

A multigrid code using Alcouffe et al. ideas [41] was adapted to have flow conservation. A volume discretization is still used to discretize the problem and the residual represents the flow balance through a cell centered at the node  $(i, j)$  where the pressure is evaluated. To eliminate the residual it is possible to act on the pressure or on the equivalent oil level. This is done in agreement with the physics of the problem for more details see Ref. [42]. This enables one to build a satisfying mono-grid discretization scheme that correctly describes the

flow behavior through an elementary cell. Afterwards, to properly represent the flow behavior through a coarse grid cell made of four fine grid cells, many difficulties were encountered. When using multigrid techniques, the problem to be solved is written as

$$Lu = f.$$

Here, we have two options.

- Option 1: set  $f = 0$  and the unknown vector  $u$  contains  $P$  and  $Hoil$ .
- Option 2: set  $f = \partial Hoil / \partial X$  which means that the Couette part of the flow is put in the right hand side of the equation.

In the first case we need to define coarsening and refining procedures for  $Hoil$  as well as for  $P$  while in the second case this is not needed but it will be necessary to update the right hand side  $f$  on the finest grid of each V-cycle each time the value of  $Hoil$  is changed. The coarsening routines for  $f$  should induce the correct right-hand side for the coarse grid equations.

In both cases an interpolation of  $Hoil$  will be needed if FMG (full multigrid see Refs. [43,44]) is used. Option 2 is the simplest one and was the one we finally chose. In that case it was also decided not to change the free boundaries on the coarser grids. Henceforth, the coarse grid relaxation will consist in only changing the pressure in the pressurized zone.

### 3. Computing time

The convergence is not the expected convergence of a multigrid process. Convergence difficulties are located at the film reformation boundary. While the frontiers of the cavitation zone stabilized rather rapidly, the flow equilibrium is slowly reached at the film reformation boundary. The multigrid routines are efficient in solving the pressure in the non cavitated zone but the equation changes a little especially at the film reformation boundary on the fine grid and this slows down the process. However the obtained convergence is sufficiently robust and fast and allows us to study the influence of dimples in the hydrodynamical lubrication of parallel surfaces. Table 1 shows the obtained residual and computing time for a single dimple of radius 1 and depth 1 at the center of a square domain  $\Omega = [-4,4] \times [-4,4]$  for various values of the ambient pressure  $P_{amb}$  with Dirichlet conditions for a  $1024^2$  grid. Table 2 shows the obtained residual and computing time for a single dimple of radius 1 at the center of a square domain  $\Omega = [-4,4] \times [-4,4]$  for various depths with  $P_{amb} = 0.01$  and Dirichlet conditions for a  $1024^2$  grid. It takes about 40 min. Afterwards most computations will be done using a  $640^2$  grid that will ensure in each considered case that there are enough points to properly describe the dimple geometry. The computing time will then be around 10 min to get a very small residual. In the periodic case, for some texture patterns, it is also possible to work on a domain that is much smaller in the  $Y$ -direction (see 7.2) and this will greatly diminish the calculation time. It seems that the cavitation boundary is rapidly found but then, especially at film reformation, the oil film level and henceforth the pressure distribution are slow to converge. In Fig. 2, the dimple and the cavitation zone obtained for various values of  $P_{amb}$  are shown. The convergence seems to depend on the height of the jump for the oil film when it reforms. It also corresponds to the proximity of the frontier at film reformation with the

Table 1

Computing time, average residual (res) and load carrying capacity (LCC) for a  $1024^2$  grid on  $[-4,4] \times [-4,4]$ , single dimple of radius 1 and depth 1 at the center.

$P_{amb}$	0.1	0.05	0.01	0.005	0.001
Time	34s	2180s	2229s	2214s	2297s
Res	$1.69 \cdot 10^{-17}$	$2.94 \cdot 10^{-12}$	$2.99 \cdot 10^{-12}$	$4.95 \cdot 10^{-13}$	$6.32 \cdot 10^{-14}$
LCC	$-2.403 \cdot 10^{-13}$	$-1.108 \cdot 10^{-2}$	$-1.466 \cdot 10^{-2}$	$-9.211 \cdot 10^{-3}$	$-2.397 \cdot 10^{-3}$

**Table 2**  
: Computing time, average residual and LCC for a 1024<sup>2</sup> grid on  $[-4,4] \times [-4,4]$ , single dimple of radius 1 at the center,  $P_{amb} = 0.01$ .

Depth	1	0.5	0.2	0.1
Time	2229s	2224s	2215s	2302s
Residual	$2.99 \cdot 10^{-12}$	$4.25 \cdot 10^{-13}$	$3.98 \cdot 10^{-14}$	$2.00 \cdot 10^{-15}$
LCC	$-1.466 \cdot 10^{-2}$	$-1.166 \cdot 10^{-2}$	$-6.807 \cdot 10^{-3}$	$-2.707 \cdot 10^{-3}$

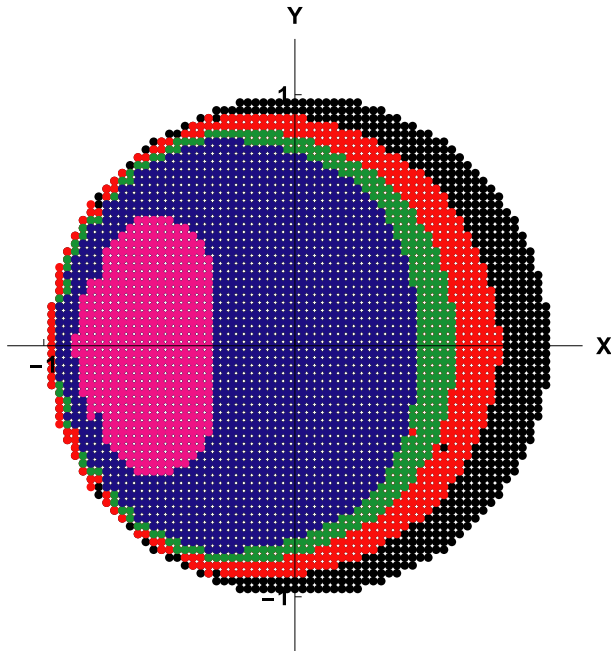


**Fig. 2.** : Dimple section (black) and cavitation zones for a dimple of radius 1, depth 1 at the center of  $\Omega = [-4,4] \times [-4,4]$  for  $P_{amb} = 0.001, 0.005, 0.01, 0.05$  in red, green, blue and pink. (For interpretation of the references to colour in this figure legend, the reader is referred to the Web version of this article.)

**Table 3**  
: Computing time, average residual and LCC for various level with a 8<sup>2</sup> coarse grid on  $[-4,4] \times [-4,4]$ , single dimple of radius 1 and depth 1 at the center,  $P_{amb} = 0.01$ .

Level	8	7	6	5
Time	2229ss	468s	99s	22s
Residual	$2.99 \cdot 10^{-12}$	$9.98 \cdot 10^{-13}$	$9.28 \cdot 10^{-15}$	$2.23 \cdot 10^{-18}$
LCC	$-1.466 \cdot 10^{-2}$	$-1.468 \cdot 10^{-2}$	$-1.468 \cdot 10^{-2}$	$-1.470 \cdot 10^{-2}$

middle of the dimple. Without cavitation (high ambient pressure or very small or very large depth or small dimple radius), the algorithm recovers the multigrid efficiency and solution only takes a few seconds. This is illustrated in Table 1 with  $P_{amb} = 0.1$ . In these Tables, LCC stands for the load carrying capacity and corresponds to the integral of  $P - P_{amb}$  over the domain. It can be noted that the load carrying capacity is always negative for a centered dimple. An explanation is provided in section 5. Table 3 shows the grid convergence of the load carrying capacity: the LCC has a relative accuracy of 0.1%.

#### 4. Generated pressure and oil film

In this section some figures of the pressure and oil film obtained for several dimple configurations are shown. In the chosen examples  $P_{amb} = 0.01$ . Fig. 3 shows the results for a single dimple of depth  $A = 1$  and radius  $R = 1$  in the domain  $\Omega = [-4,4] \times [-4,4]$  whose center is located at  $(X_i, Y_i) = (-2,0)$ . The geometry is given in Fig. 3(a): the

dimple is located at the center of the first half of the domain. The resulting pressure is given in Fig. 3(c) and (d) respectively in the Dirichlet and periodic cases. The pressure rapidly decreases towards the cavitation pressure inside the dimple. At the dimple exit which corresponds to the convergent part of the surfaces, it grows very rapidly to reach its maximum value. In Fig. 3(b), the equivalent oil level is given for the Dirichlet case. In the cavitation zone the representation is not adequate since, in reality, there is a mixture of gas, oil and vapor. We have decided to represent an equivalent oil level that is to say  $H_{oil} = \theta H$  where  $\theta$  is the filling ratio. The oil flow inside the dimple before cavitation can be viewed. Inside the cavitation zone it remains constant in the X-direction. At the exit of the dimple, where the film reforms, a discontinuity can be observed. The full film zone inside the dimple is narrow around the dimple edges. Fig. 5 shows the geometry, the oil level and the pressure for a set of nine dimples of depth  $A = 1$  and radius  $R = 1$  in the domain  $\Omega = [-10,10] \times [-10,10]$  whose center is located at  $(X_i, Y_i) = (-2,0)$ . The dimple pattern is also shown in that figure. In each dimple the pressure shows the same behavior as in a single dimple but at the exit of the first 2 rows of dimples the pressure does not reach very high values since rapidly it will decrease towards cavitation because of the next row of dimples. The maximum pressure is reached at the exit of the last row of dimples because afterwards no cavitation occurs. Here the limitation is mainly given by the exit boundary condition and therefore depends on the distance to the contact exit. Related results can be seen on the oil film. The last row of dimples is the fullest of the three. The main difference between the Dirichlet and the periodic case lies in the fact that the pressure does not reach the ambient pressure on the Y-boundaries enlarging the zone where the pressure is above the ambient pressure in the case of a dent or a pattern of dents in the contact inlet or enlarging the zone of pressure smaller than the ambient pressure in the case of a texture in the contact outlet. It may be noticed that the cavitated areas are not significantly different in those 2 cases as shown in Fig. 4. Henceforth it seems that the distance of the dimple to the boundaries and the boundary conditions must have a large influence on the load carrying capacity.

### 5. Load carrying capacity

#### 5.1. Influence of the textured area on the load carrying capacity

The load carrying capacity is defined as:

$$LCC = \int_{\Omega} (P - P_{amb}) dX dY. \quad (8)$$

When the dimples are near the inlet, the load carrying capacity is positive and then it becomes negative as noticed by many authors. Considering a single dimple, it may be noted that the pressure will first decrease. This decrease will be limited by the cavitation pressure. To conserve the flow, oil must enter the dimple leading to the “inlet suction” phenomenon. Afterwards, in the convergent part of the dimple, the pressure will rise again starting from a point determined by the extra oil inside the dimple and then it will decrease to reach the ambient pressure at the contact exit. If the dimple is situated near the contact entrance, the zone where the pressure is less than the ambient pressure is limited and if it is located near the exit, the zone where it is above the ambient pressure is more limited. Besides, in case of cavitation, the pressure is not anti-symmetric with respect to  $P_{amb}$  and if  $P_{max}$  denotes the maximum pressure,  $P_{max} - P_{amb}$  is usually higher than  $P_{amb} - P_{cav}$ . This is illustrated in Fig. 6 where, on each row, the middle figure shows the part of the pressure above  $P_{amb}$  while the last one shows the part of the pressure below the ambient pressure to highlight the zone where the pressure is less than the ambient pressure. In the last figure we have plotted  $-P$  and  $-P_{amb}$ . Again it may be noted that in the case of a dent in the inlet, the zone of pressure above  $P_{amb}$  significantly increases.

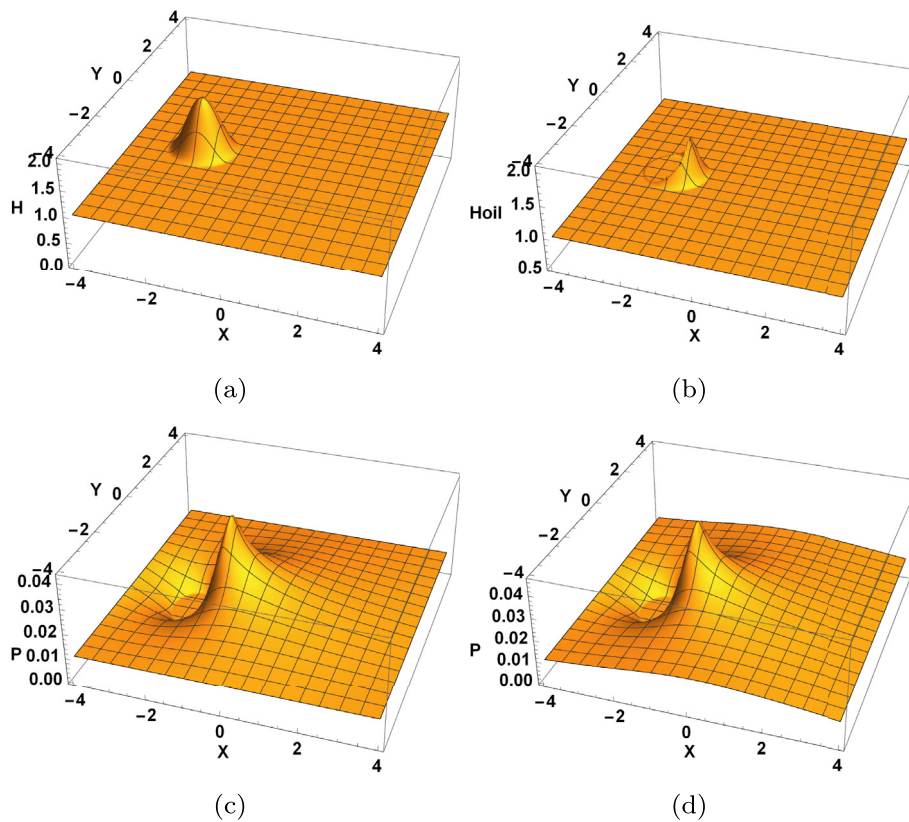


Fig. 3. Pressure and oil film generated on  $[-4,4] \times [-4,4]$  by a single dimple of depth 1 centered at  $(-2,0)$ . (a) Geometry, (b) Film height, (c) Pressure (Dirichlet), (d) Pressure (periodic).

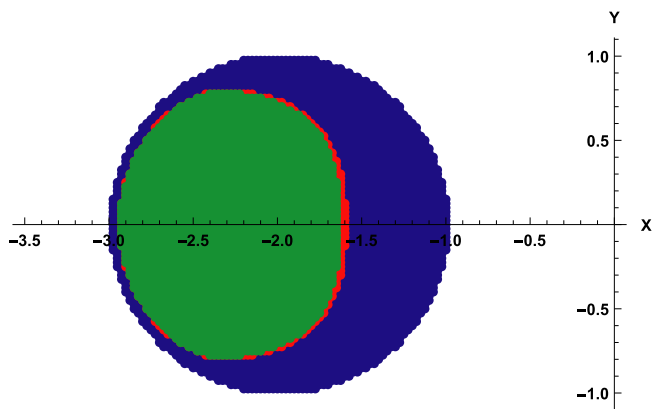


Fig. 4. Cavitation zone: zone inside the dimple (blue disk), cavitation zone: Dirichlet (red + green), Periodic green. (For interpretation of the references to colour in this figure legend, the reader is referred to the Web version of this article.)

If the texture symmetrically covers the domain the generated load carrying capacity becomes zero in case of no cavitation and negative otherwise. Hence partial texturing is needed to induce a positive load. To illustrate this, rows of three dimples of depth 1 spaced by 4 centered at  $X_i = -18, Y_i = 0$ , then  $X_i = -16, Y_i = 0$ , then  $X_i = -14, Y_i = 0$ , etc ... up to  $X_i = 18, Y_i = 0$  where they cover the whole domain  $\Omega = [-20,20] \times [-20,20]$  in the X-direction were progressively added and the generated load was computed. The pressure distribution can be viewed in Fig. 7. It can be noticed that at the exit of each row the pressure progressively increases except in the last figure where the whole range of values in X is covered. The largest pressures are obtained on the last row of dimples when the dimples remain in the first part of the domain. The load carrying capacity in terms of the number,

$N$ , of dimple rows is shown in Fig. 8. The maximum load carrying capacity is obtained with 3 rows of dimples in the inlet of the contact. When adding more rows it rapidly decreases to reach a negative value when the entire domain is covered. When rows are added at the end of the contact, there is always a loss in LCC. The variations in LCC are more limited than when rows are added in the inlet. The behavior of the maximum pressure is also quite different. Considering the different behaviors of the load carrying capacity and of the maximum pressure according to whether the inlet or the outlet is textured (see Figs. 7 and 8), it can be noticed that the loss of load carrying capacity when the outlet is textured is lower than the gain when the inlet is textured. The maximum pressure is much higher if the inlet is textured rather than the outlet and its variations are also less important. For a one-dimensional simple model, Fowell et al. [11] show that  $P_{max} \approx P_{amb}L/\Delta$  where  $L$  is the contact length and  $\Delta$ , the distance of the pocket to the inlet. Here it seems that a similar trend can be observed. It can be noticed that in the periodic case these effects are increased due to the larger zone where the pressure is greater than the ambient pressure. In the periodic case the maximum LCC is roughly twice the maximum LCC in the Dirichlet case. The size of the domain in the direction that is perpendicular to the sliding direction probably plays an important part in this phenomenon. Besides, in the periodic case the flow remains constant.

### 5.2. Partial texturing at both ends

Because of the previous remarks, it may be worthwhile for reciprocating contacts to have partial texturing at both ends of the contact. This type of partial texturing for piston rings was experimentally tested by Ryk and Etsion [45] and Etsion and Sher [46]. Tomanik [10] also investigated that kind of partial texturing but using a 1D code without mass-conservation. In 2016, Shen and Khonsari [37] have also conducted experimental as well as numerical studies with a mass-conserving algorithm and for the transient case on the effects of different

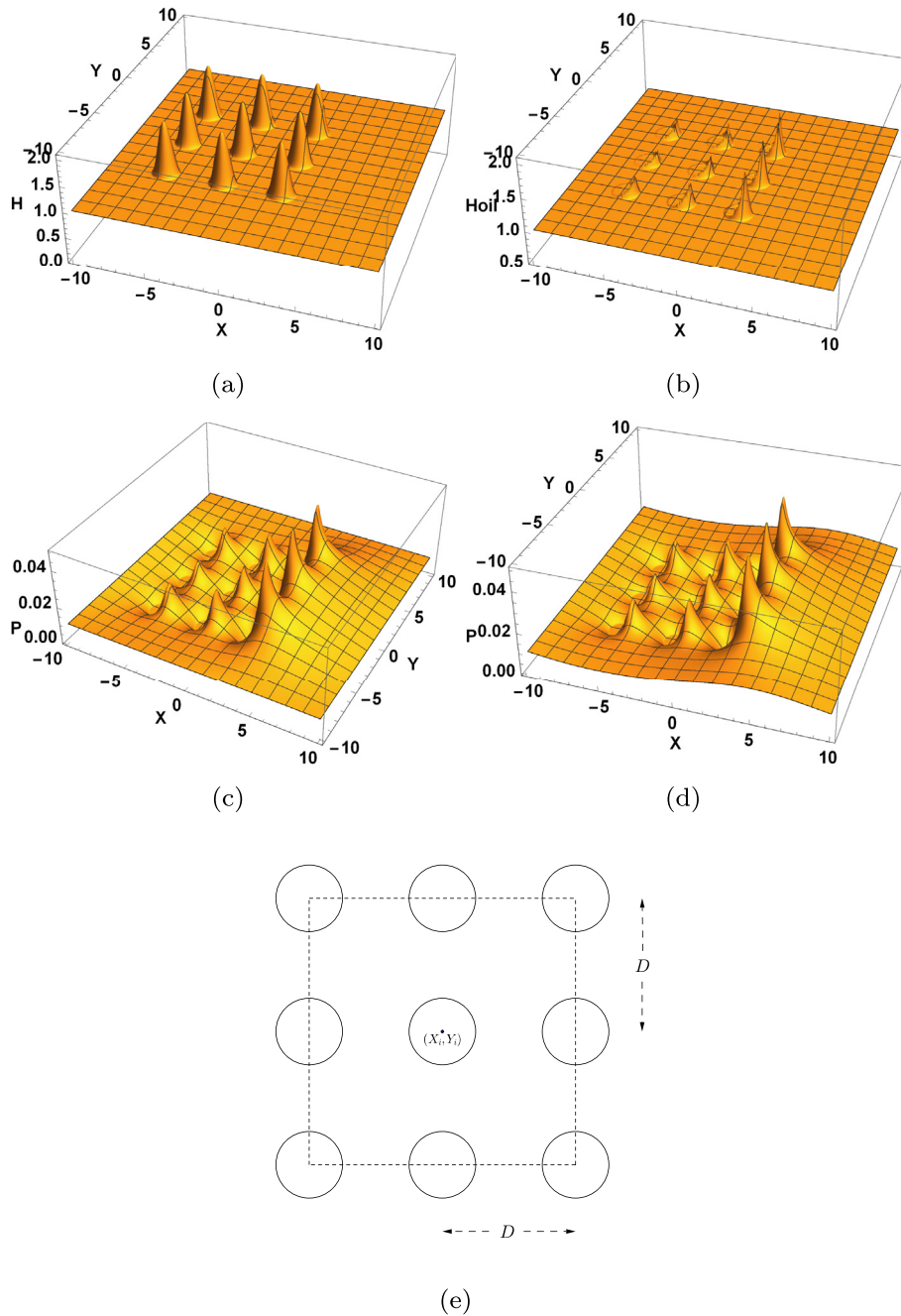


Fig. 5. Pressure and oil film generated on  $[-10,10] \times [-10,10]$  by a pattern of 9 dimples of depth 1 and spaced by  $D = 4$  centered at  $(-2,0)$ . (a) Geometry (b) Film height (Dirichlet) (c) Pressure (Dirichlet), (d) Pressure (periodic) (e) Nine dimple pattern.

positions of pockets (rather patches of micro-dimples) in the inlet and in the outlet for a flat piston ring. Tala-Ighil, Fillon and Maspeyrot [33] have also tested various configurations of patches of dimples but for a hydrodynamic journal bearing. As can be seen in Fig. 9, a positive load carrying capacity is always generated. Its value is indicated for each case on the corresponding image of the pressure distribution. For our example the maximum load carrying capacity is obtained for two rows of indents at both ends. The maximum pressure is obtained at the exit of the last row of indents in the inlet. It will reach a sufficiently high value if the distance between the 2 sets of dimples is large enough and if the first set of dimples lies sufficiently near the inlet boundary inducing a total positive load carrying capacity. Fig. 10 shows similar results with similar conclusions for the periodic case.

### 5.3. Load carrying capacity in terms of the texture location

The behavior of the load carrying capacity in terms of the position of the set of dimples along the line  $Y = 0$  is now studied. In Fig. 11, the results are shown for  $\Omega = [-10,10] \times [-10,10]$  and for  $\Omega = [-20,20] \times [-20,20]$  for a pattern of nine dimples of radius 1, depth 1 and equally spaced by 4. The load carrying capacity becomes negative when the texture approaches the middle of the contact. A linear behavior is observed in the center of the domain although this is less clear on the smaller domain. In that case, the domain is not large enough to ensure that no dimple is close to the inlet or the outlet of the contact. Close to the boundaries and especially near the inlet, the dimple influence becomes non linear. The maximum pressure and the size of the zone behind the texture induce the positive part in the load carrying

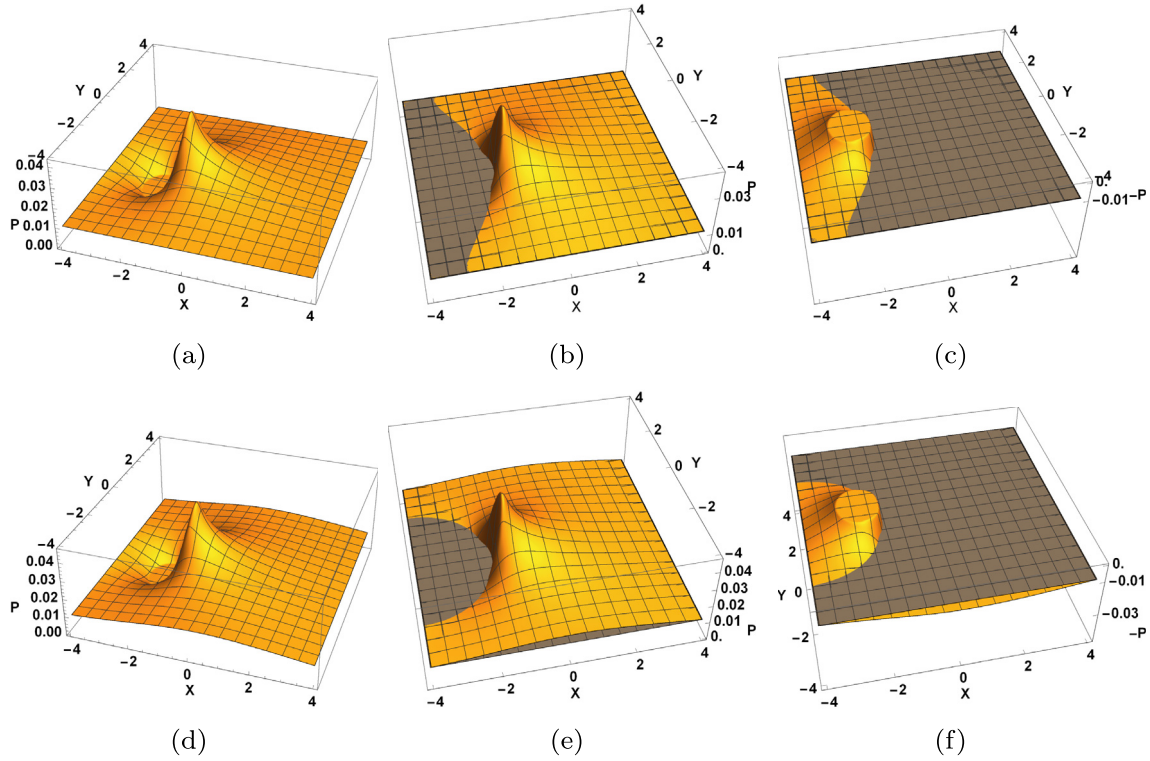


Fig. 6. : (a, d) Pressure generated on  $[-4,4] \times [-4,4]$  by a single dimple of depth 1 centered at  $(-2,0)$ . (b, e) Part above the ambient pressure (c, f) Part below the ambient pressure (Here  $-P$  and  $-P_{amb}$  are plotted). First row: Dirichlet case, second row: periodic case.

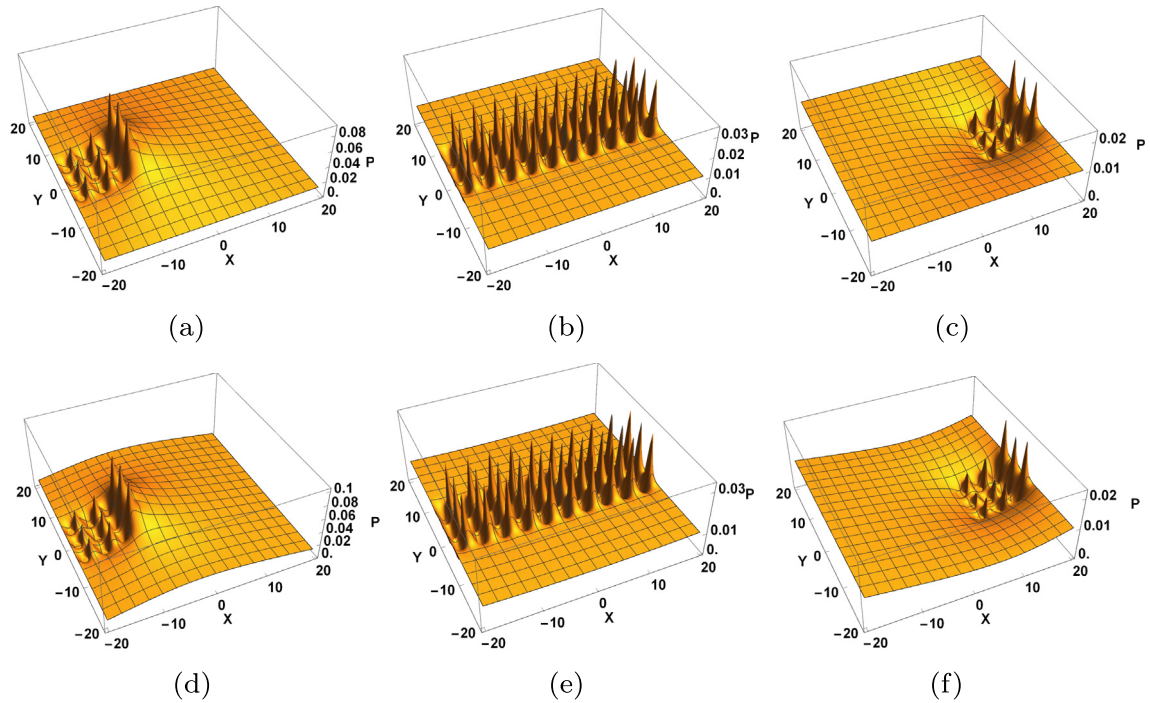


Fig. 7. Pressure generated on  $[-20,20] \times [-20,20]$  as a function of the number of rows of 3 dimples of depth 1 in the inlet or in the outlet. Left: 3 rows in the inlet - Middle: 10 rows - Right: 3 rows in the outlet. First row: Dirichlet conditions - Second row: periodic conditions.

capacity while the cavitation pressure and the size of the zone ahead the texture determine the negative part.

### 6. Homogenization

In this section it is shown that the behavior of a pattern of dimples

can be investigated using a single well chosen dimple. Choosing  $\Omega = [-10,10] \times [-10,10]$ , we tried to replace the previous pattern of nine dimples by a square dimple. The volume of the chosen dimples (see equation (7)) of radius  $R$  and depth  $A$  is given by  $V = AR^2(\pi/2 - 2/\pi)$ . We considered a single rectangular dimple of the same volume and the same center as the nine dimples. We had two obvious choices for that

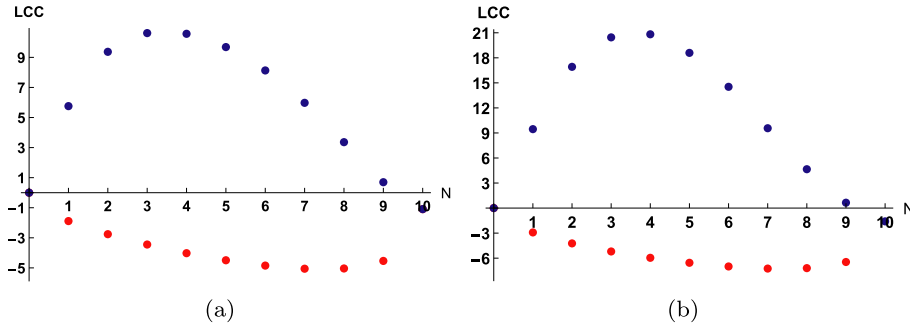


**Fig. 8.** Load carrying capacity as a function of the number  $N$  of rows of three dimples of depth 1 spaced by  $D = 4$  on  $\Omega = [-20,20] \times [-20,20]$ . In blue the first row is located at  $(-18,0)$ , in red the last row is located at  $(18,0)$ . (a) Dirichlet - (b) Periodic. (Note the different vertical axes.). (For interpretation of the references to colour in this figure legend, the reader is referred to the Web version of this article.)

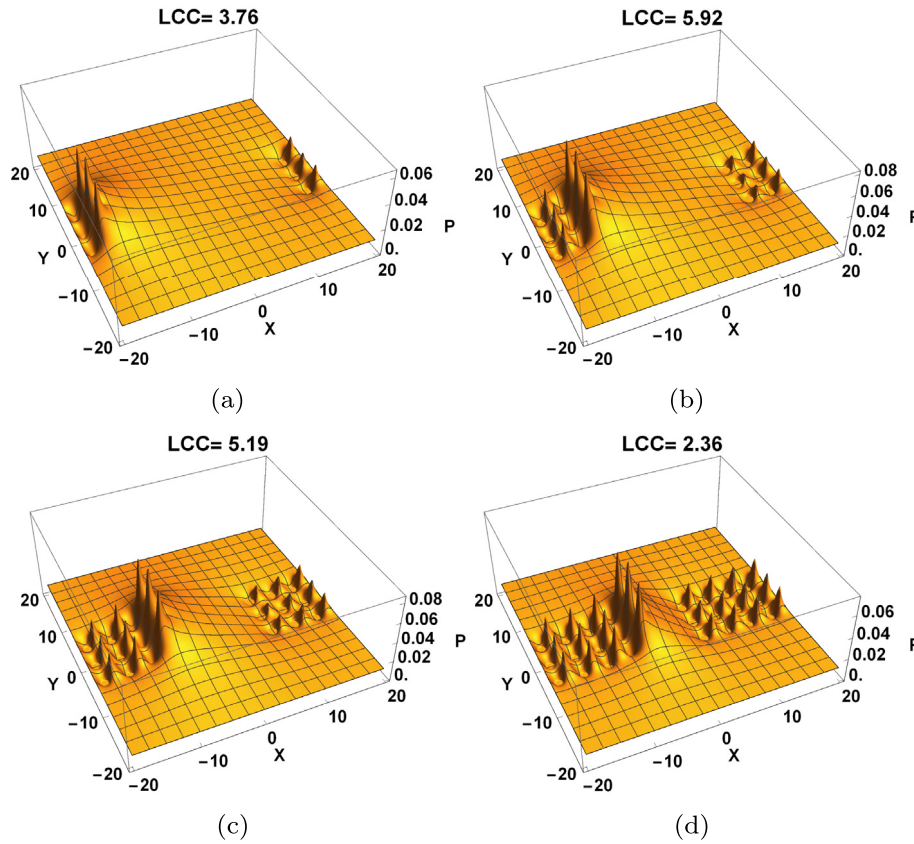


**Fig. 9.** Dirichlet case: Pressure generated on  $[-20,20] \times [-20,20]$  with  $N$  rows of 3 dimples of depth 1 spaced by 4 at both ends,  $P_{amb} = 0.01$ . (a)  $N = 1$  (b)  $N = 2$  (c)  $N = 3$  (d)  $N = 4$ .

square: a  $10 \times 10$  square corresponding to the smallest square containing all dimples or a  $8 \times 8$  square passing through the centers of the external dimples. Both were tried and results are shown in Fig. 12. The square of size 10 is the best choice in the inlet while the square of size 8 is better in the outlet. Similar trends as for step bearings are observed (see Fig. 13).

Another comparison with the results shown in Figs. 7–9 was done by considering rectangular dimples of the same volume as the dimple patterns tangent to the external dimples (see 13).

Results can be viewed in Figs. 14–16. Similar behavior can be observed but with a roughly doubled load carrying capacity. Again in the periodic case, larger load carrying capacity than in the Dirichlet case is generated. Here too the maximum LCC is roughly doubled (from Dirichlet to the periodic case) as with the pattern of dimples. The flow and therefore the load carrying capacity is influenced by the geometry. The flow behavior depends on the “conductance” values generated by the

geometry. These conductances defined by  $H^3$  have been evaluated for the two geometries, rows of three dimples and equivalent rectangular dimples. Using conductance rules, the ratio of the additional conductance  $CR$  generated by the equivalent rectangular dimple and the dimples was computed.

$$CR(N) = \frac{\text{Equivalent rectangular dimple conductance} - H_0^3}{\text{Dimple row conductance} - H_0^3} \quad (9)$$

With our discretization, the conductance is computed by  $\sum_j \frac{1}{\sum_i H_{i,j}^3}$ .

In the smooth case, it simplifies to  $H_0^3$ . The values are given in Table 4. It shows a ratio around 1.8. The other columns of the table show the values that are obtained by multiplying the LCC for a row of three dimples and the LCC for the associated rectangular dimple of the same volume for the periodic case (columns 3 and 4) and for the Dirichlet case (columns 5 and 6). For a number  $N$  of rows between 2 and 5, there

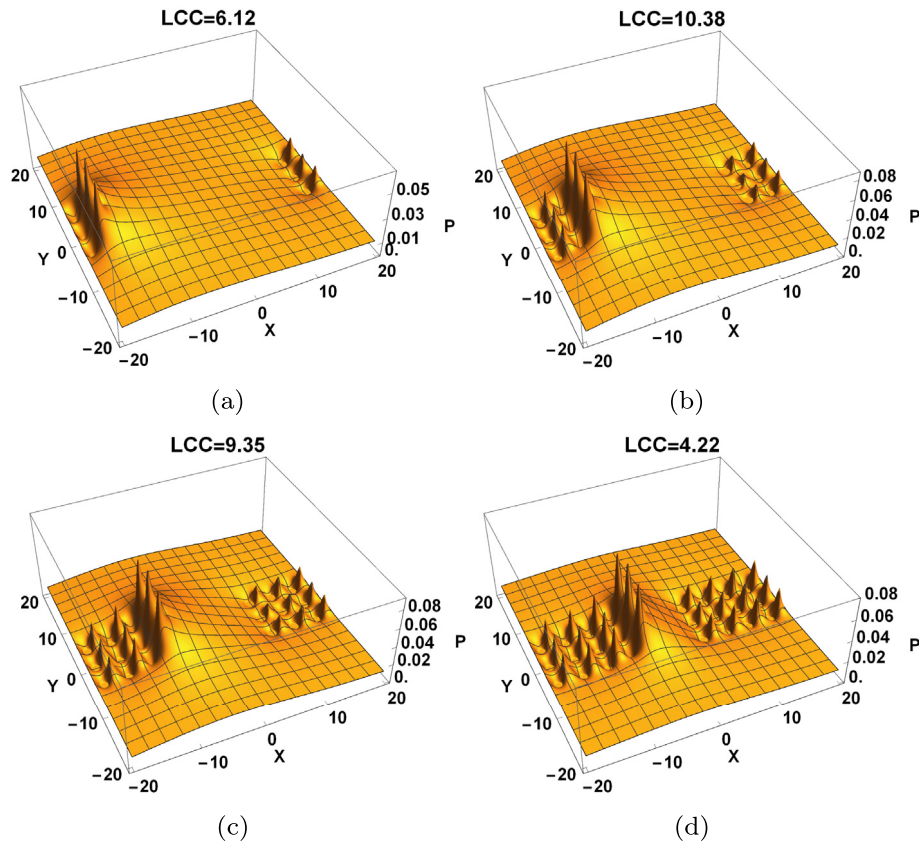


Fig. 10. Periodic case: Pressure generated on  $[-20,20] \times [-20,20]$  with  $N$  rows of 3 dimples of depth 1 spaced by 4 at both ends,  $P_{amb} = 0.01$ .(a)  $N = 1$  (b)  $N = 2$  (c)  $N = 3$  (d)  $N = 4$ .

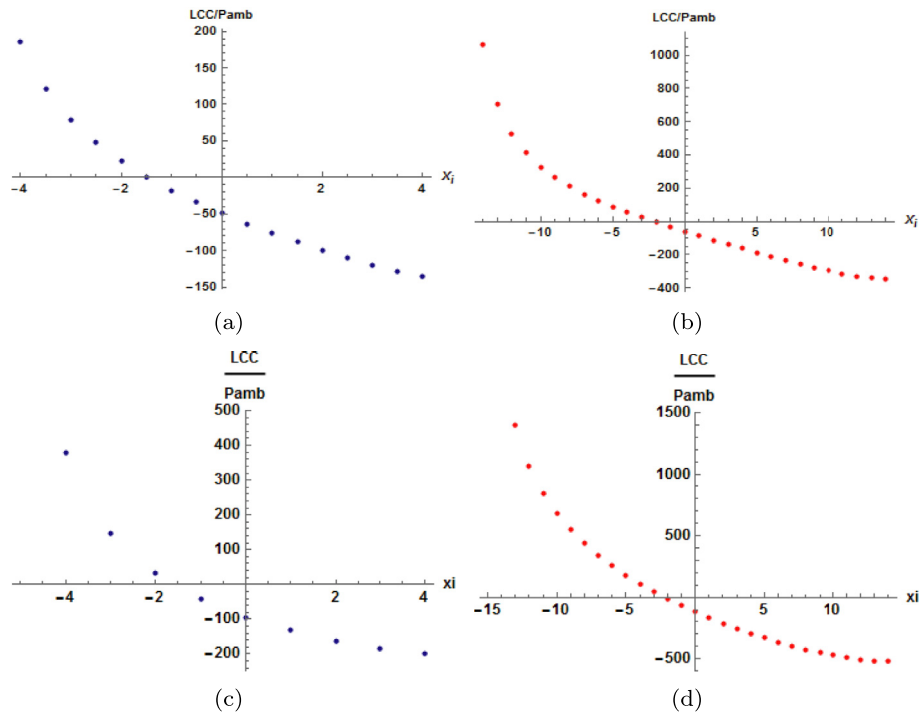


Fig. 11. Load carrying capacity generated by a pattern of nine dimples of depth 1 spaced by 4 as a function of the position of the center of the pattern on the line  $Y = 0$ .(a) and (c)  $\Omega = [-10,10] \times [-10,10]$  - (b) and (d)  $\Omega = [-20,20] \times [-20,20]$ . First Row: Dirichlet case - Second row: periodic case.

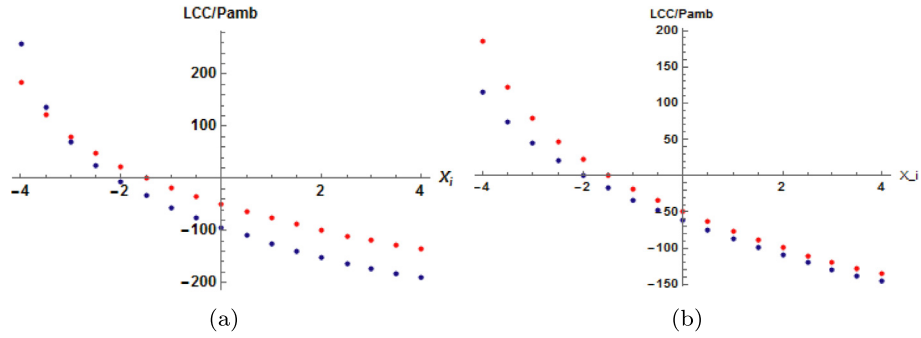


Fig. 12. Dirichlet case: Load carrying capacity of a square dimple of identical volume as the nine indent pattern (in blue) compared with the load carrying capacity (in red) of the pattern of nine dimples of depth 1 spaced by 4 on  $\Omega = [-10,10] \times [-10,10]$ , (a) a square dimple of size 10, (b) a square dimple of size 8. (For interpretation of the references to colour in this figure legend, the reader is referred to the Web version of this article.)

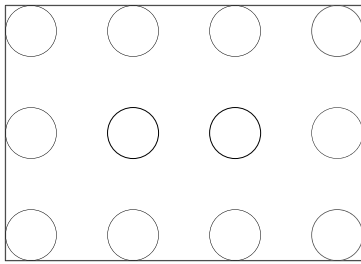


Fig. 13. Section of a rectangular dimple equivalent to 4 rows of 3 dimples.

is less than 10% difference.

this case the dimensionless Reynolds equation reads:

$$\frac{\partial}{\partial X} \left( H^3 \frac{\partial P}{\partial X} \right) - \frac{\partial(H_{oil})}{\partial X} = 0 \quad (10)$$

In Fig. 18, the step bearing is represented in black. The red line represents the pressure distribution in the case of cavitation.  $P_0$  corresponds to  $P_{amb}$ .

In the 1D case analytical formulas for the pressure and the oil film can easily be found using flow conservation. In case of cavitation and fully flooded conditions, the following results are obtained:

$$\begin{aligned} P(X) &= P_0(1 - (X - X_0)/l) & H_{oil} &= H_0 & X &\in [X_a, X_1] \\ P(X) &= P_{cav} = 0 & H_{oil} &= H_0 + H_0^3 P_0/l & X &\in [X_1, X_r] \\ P(X) &= P_{max}(X - X_r)/(X_2 - X_r) & H_{oil} &= H_0 + A & X &\in [X_r, X_2] \\ P(X) &= (P_{max} - P_0)(X_b - X) & H_{oil} &= H_0 & X &\in [X_2, X_b] \\ & & & & & / (X_b - X_2) + P_0 \end{aligned} \quad (12)$$

## 7. Comparison with the behavior of one dimensional step bearing

### 7.1. Analytical results for a one dimensional step bearing

The 1D geometry and the notations used are described in Fig. 17. In

with

$$P_{max} = P_0(1 + L/l)$$

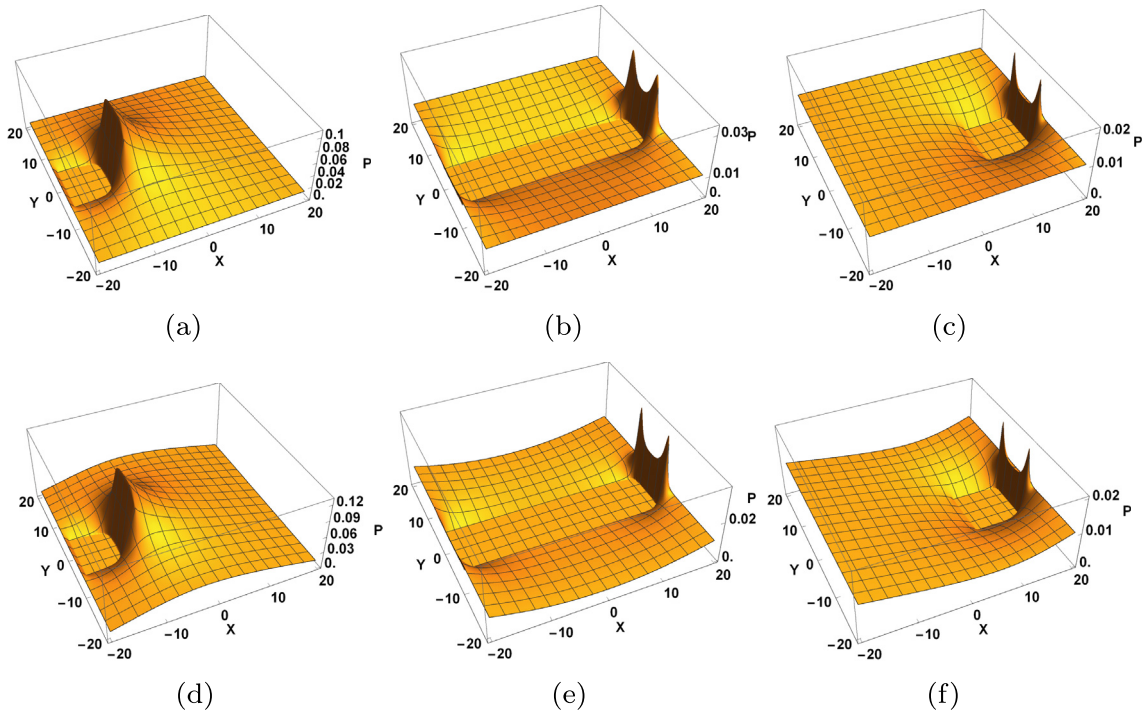


Fig. 14. Pressure generated on  $[-20,20] \times [-20,20]$  with an equivalent rectangular dimple of position similar to the indent position of Fig. 7. First row: Dirichlet conditions - Second row: periodic conditions.

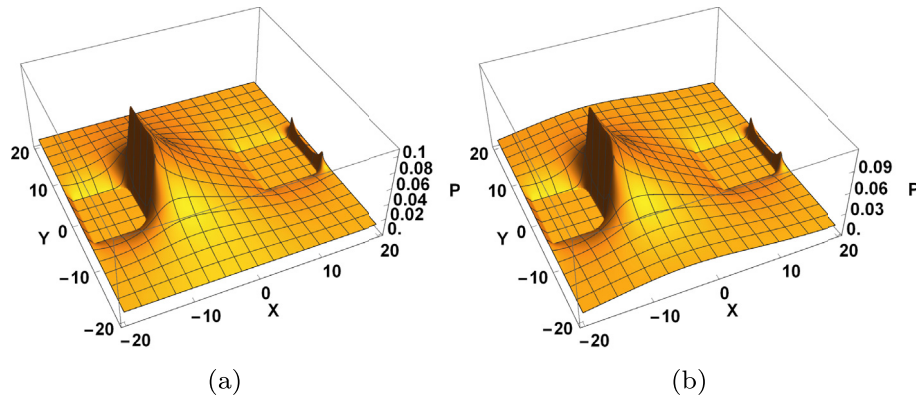


Fig. 15. Pressure generated on  $[-20,20] \times [-20,20]$  with an equivalent rectangular dimple of position similar to the indent position of Fig. 9. (a) Dirichlet (b) Periodic.

and

$$X_r = X_2 + P_{max}(H_0 + A)^3 / (H_0^3 P_0 / l - A)$$

It may be noted that the maximum pressure does not depend on  $A$ , the step depth. The influence of  $A$  results from the position  $X_r$  of the film reformation boundary. Similarly, in the non cavitated case, the following results are obtained:

$$\begin{aligned} P(X) &= P_0(X_1 - X)/l + P_{min}(X - X_a)/l & H_{oil} &= H_0 & X &\in [X_a, X_1] \\ P(X) &= P_{min}(X_2 - X)/l_s + P_{max}(X - X_1)/l_s & H_{oil} &= H_0 + A & X &\in [X_1, X_2] \\ P(X) &= P_{max}(X_b - X)/L + P_0(X - X_2)/L & H_{oil} &= H_0 & X &\in [X_2, X_b] \end{aligned} \quad (14)$$

with, for  $H_0 = 1$ ,

$$P_{min} = P_0 - ll_s A / (l_s + (l + L)(1 + A)^3)$$

and

$$P_{max} = P_0 + Ll_s A / (l_s + (l + L)(1 + A)^3)$$

In this case,  $P_{min}$  and  $P_{max}$  depend on  $A$ . There is no cavitation if  $P_{min}$  is positive, that is to say if  $ll_s A / (l_s + (l + L)(1 + A)^3) < P_0$ . Therefore if  $P_0 = P_{amb}$  is sufficiently large or  $A$  sufficiently small or sufficiently large there is no cavitation. This is also true in the 2D case. These analytical results can be used to validate our code in Fig. 18, the numerical pressure (in blue) and the analytical pressure in (red) are represented together. The two curves superimpose.

An analytical expression of the load carrying capacity can easily be deduced from the above expression of the pressure. In the cavitated case when the cavitation is important enough, it can be approximated by the following expression:

$$LCC \approx P_0 \left( -\frac{l}{2} - l_s + \frac{L^2}{2l} \right) = P_0 \left( X_a - X_b + 0.5 \frac{(X_b - X_a - l_s)^2}{X_{mil} - X_a - 0.5l_s} \right) \quad (15)$$

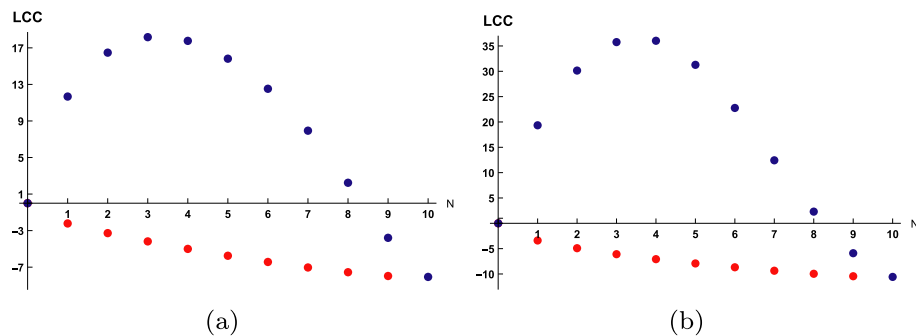


Fig. 16. Load carrying capacity for equivalent volume rectangular dimple in terms of the number  $N$  of associated rows of three dimples of depth 1 spaced by  $D = 4$  on  $\Omega = [-20,20] \times [-20,20]$ . In blue the first row is located at  $(-18,0)$ , in red the last row is located at  $(18,0)$ . (a) Dirichlet, (b) Periodic. (Note the different axes.). (For interpretation of the references to colour in this figure legend, the reader is referred to the Web version of this article.)

Table 4

Conductance ratio between equivalent volume rectangular dimple and  $N$  rows of three dimples.

N	Conductance ratio	CR(N) × LCC		LCC	
		N Rows of 3 dimples	equivalent rectangular dimples	N Rows of 3 dimples	equivalent rectangular dimples
		Periodic	Periodic	Dirichlet	Dirichlet
1	1.68	15.9	19.3	9.7	11.7
2	1.79	30.3	30.1	16.8	16.5
3	1.81	37.0	35.8	19.2	18.2
4	1.82	37.9	36.0	19.2	17.8
5	1.81	33.7	31.3	17.5	15.8
6	1.80	26.2	22.8	14.7	12.5
7	1.79	17.1	12.4	10.7	7.9
8	1.78	8.3	2.3	6.0	2.2
9	1.77	1.1	- 5.9	1.2	- 3.8
10	1.76	- 2.8	- 10.5	- 1.9	- 8.1

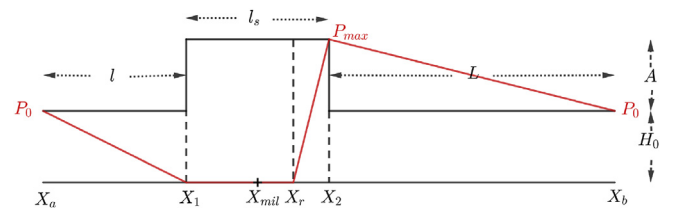


Fig. 17. One dimensional step bearing: in black, geometry and in red pressure (cavitated case). (For interpretation of the references to colour in this figure legend, the reader is referred to the Web version of this article.)

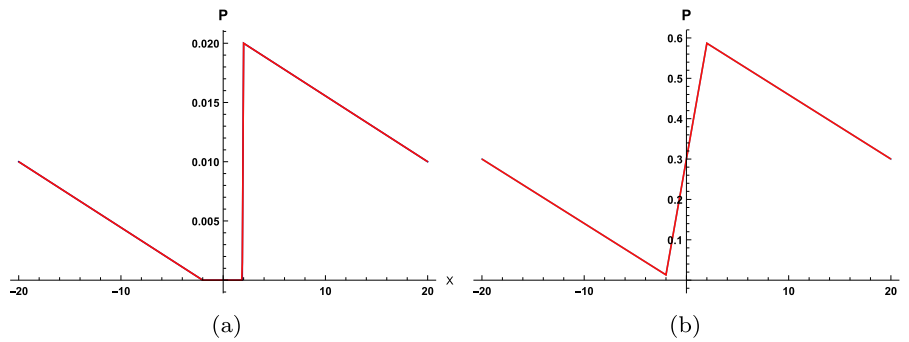


Fig. 18. Computed 1D pressure (in red) generated by a step bearing of length 4 of depth 0.5 located at the center of the contact together with the analytical pressure (in blue) in  $\Omega = [-20,20]$ . (a) Cavitated case  $P_{amb} = 0.01$ , (b) Non cavitated case  $P_{amb} = 0.3$ . (For interpretation of the references to colour in this figure legend, the reader is referred to the Web version of this article.)

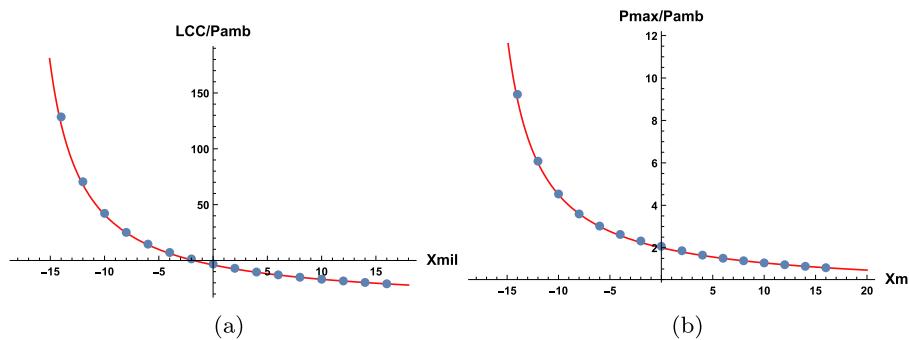


Fig. 19. Computed 1D load carrying capacity (left, blue dots) and maximum pressure (right, blue dots), generated by a step bearing of length 4 of depth 0.5 as a function of the position of its middle point along the contact together with the analytical approximated functions (red curve) on  $\Omega = [-20,20]$  in the cavitated case for  $P_{amb} = 0.01$ . (For interpretation of the references to colour in this figure legend, the reader is referred to the Web version of this article.)

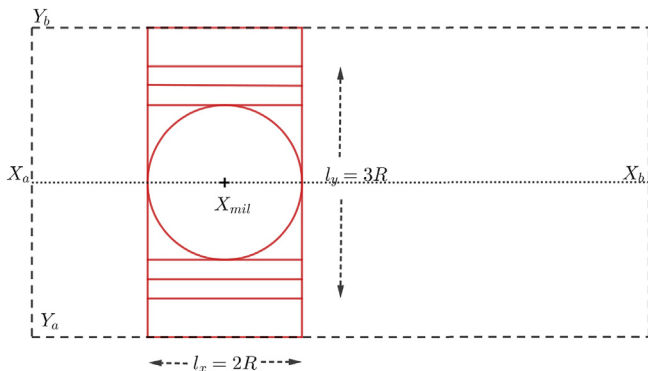


Fig. 20. Schematic view of the step bearing, and the section of the circular dimple of radius  $R$  and rectangular dimples of sides  $l_x$  and  $l_y$  on  $\Omega = [X_a, X_b] \times [Y_a, Y_b]$ .

Where  $X_{mil}$  is the position of the middle of the step bearing. It may be noted that this approximated value does not depend on the step bearing depth. The curve of the approximated LCC as a function of the position of the middle of the step and computed values are shown in Fig. 19. There is a good agreement between them. One also notes a good agreement between the calculated results and predicted values for the maximum pressure (see Fig. 20).

### 7.2. Comparison with two dimensional numerical results for a single dimple in the periodic case

Numerical 2D calculations were performed for the periodic case to determine the difference in LCC capacity generated by a row of dents in the  $Y$ -direction and an equivalent rectangular dimple of the same volume. Because of the periodicity it is sufficient to consider a single

dimple. Four types of dimples were considered: our basic circular dimple of depth  $A = 1$  of radius  $R = 1$  and rectangular dimples of the same volume of section  $l_x = 2R, l_y = 2R, 2.5R, 3R$  centered on the line  $Y = 0$ .

The domain  $\Omega$  on which calculations were performed is  $\Omega = [-20,20] \times [-2,2]$ . The final LCC is divided by the domain width for comparison with the 1D results. Results are shown in Fig. 21.

It can be noted that the 1D model provides a good approximation of the LCC behavior after the first quarter of the domain. There is an

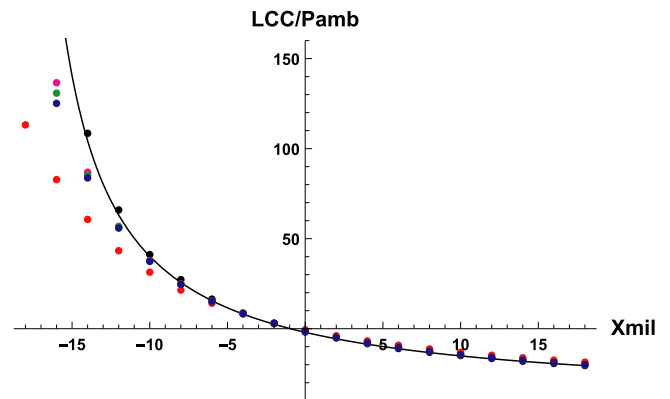


Fig. 21. On  $\Omega = [-20,20] \times [-2,2]$  in the cavitated case for  $P_{amb} = 0.01$  and  $R = 1$ , computed load carrying capacity for a circular dimple of radius  $R = 1$ , depth  $A = 1$  (red dots) together with the LCC generated by a step bearing of size  $l_x = 2R, l_y = 4$  (black dots), rectangular dimples of sizes  $l_x = 2R$  and  $l_y = 2R, 2.5R, 3R$  (pink, green and blue dots) of the same volume with the analytical solution (black curve) as a function of the position of its middle point along the contact. (For interpretation of the references to colour in this figure legend, the reader is referred to the Web version of this article.)

**Table 5**  
Load Carrying capacity in the case of partial texturing with patterns of  $N$  rows of three dimples in the inlet and in the outlet of the contact.

$N$	Dimensionless LCC	Dimensional total LCC
1	6.12	2.07 N
2	10.38	3.50 N
3	9.35	3.16 N
4	4.22	1.42 N

**Table 6**  
: Load Carrying capacity in the case of partial texturing with patterns of  $N$  rows of ten dimples in the inlet and in the outlet of the contact.

$N$	Dimensionless LCC	Dimensional total LCC
1	33.26	11.23 N
2	60.80	20.52 N
3	41.02	13.84 N
4	10.50	3.54 N

asymptotic line corresponding to the position of  $X_{mil}$  for which the dimple starts to completely lie in the contact. Before this position, the analytical approximated value is not valid. The approximation is much better with rectangular dimples and of course also better when they get larger in the  $Y$ -direction becoming closer to the 1D case. The geometry of the dimple seems to affect the LCC mostly in the contact inlet.

### 7.3. Dimensional results

For a viscosity  $\eta = 0.02$  Pa.s, a mean velocity  $u_m = 5$  m/s, a clearance  $h_0 = 1$ .  $\mu\text{m}$ , a contact width  $x_b - x_a = 0.3$  mm a ring length of 20 cm and dimples of depth  $a = 1$ .  $\mu\text{m}$  radius  $r = 7.5$   $\mu\text{m}$ , the dimensionless pressure is  $P = p/p_0$  with  $p_0 = 9$  MPa. In this case, using

## Appendix. comparison with literature results

A validation of our code was previously mentioned by comparison with the 1D analytical results in section 7.2.

Our results were also compared with the results obtained by Biboulet and Lubrecht in Ref. [29] with a code based on the Woloszynski, Podsiadko and Stachowiak [28] approach. The dimensionless domain  $\Omega$  is a square  $[-10,10] \times [-10,10]$ . They consider a pattern of 25 dents of depth  $A = 1$  spaced by  $D = 4$  and radius  $R = 1$  of center located at  $X_c$  on the central line. The comparison was made for  $P_{amb} = 0.04$  and  $X_c = 0, -1, 1$  on a  $1025 \times 1025$  grid. It was also tested for a non cavitating case  $P_{amb} = 0.4$  and  $X_c = -1$ . The dimensionless parameters are the same but [29] computes the mean value of  $P - P_{amb}$  and henceforth our results have to be divided by the domain area. Results are given in Table 7. Our results and those of [29] are converged up to machine accuracy. Hence the difference stems from the discretization schemes used. Both are second order accurate but our scheme has an error that is 3/8 of the error in Ref. [29]. This result is coherent with a grid convergence analysis performed.

Finally, our results were compared with the results obtained by Profito et al. in [27] for a textured sliding bearing. They consider parallel bearings with the characteristics described in Table 8. The dimples have a parabolic geometry. For the load carrying capacity they compute  $W = \int_{\Omega} P dX dY$ .

The stationary bearing is textured with  $N$  parallel rows of 10 dimples in the inlet spaced by  $4r$ . This texture will be denoted by  $10 \times N$ . The results are shown in Table 9

Our results are calculated up to machine precision on a  $1025 \times 1025$  grid. It leads to about 2500 nodes per local dimple cell and  $10^4$  nodes per full dimple cell instead of respectively 900 and 3600 in [27]. We keep a uniform mesh all over the domain even in the non textured area which is not the case in [27]. This can explain the observed difference which increases with increasing non textured area. However, the difference is smaller than 1% for the worst case.

the dimple radius and the clearance as dimensionless factors, we have, for  $P_{amb} = 0.01$ ,  $P_{amb} - P_{cav} = 0.09$  MPa. For a periodic pattern in the  $y$ -direction of period 0.3 mm with  $N$  rows of three dents at the inlet and at the outlet of the contact (see Fig. 10), the obtained dimensionless and total dimensional load carrying capacity are given in Table 5. For a periodic pattern in the  $y$ -direction of period 0.3 mm with  $N$  rows of 10 dents at the inlet and at the outlet of the contact, the obtained dimensionless and total dimensional load carrying capacity are given in Table 6.

## 8. Conclusion

For parallel surfaces in hydrodynamic lubrication, no pressure can be generated without a surface texture. A multigrid flow preserving algorithm is used to analyse the influence of the texture on the load carrying capacity. Partial texturing with micro dimples can induce positive pressure when the texture is located in the contact inlet. However, the loss of pressure generation is less important for the outlet texture than the gain for the inlet texture. By texturing both contact ends, a positive load carrying capacity is generated which may be useful for reciprocating contacts as for the flat ring in the piston ring cylinder liner contact. Partial texturing generates a pressure distribution similar to that of a step bearing. This behavior was analysed by comparison with a rectangular dimple of the same volume as the indent texture pattern and similar location. Higher LCC is generated by the equivalent rectangular dimple. This was explained by the influence of the geometry on the conductances. Besides in the periodic case and in the case of cavitation, the analytical LCC expression for the 1D model for a step bearing as a function of the position of the texture provides a good estimate of the load carrying capacity for dimples in the 2 dimensional case. This can provide a way of designing micro-textures for the flat ring without further calculations.

**Table 7**  
Comparison with the Biboulet and Lubrecht results in Ref. [29].

$P_{amb}$	$X_c$	[29] results	Present code results
0.04	0	$-1.0458 \cdot 10^{-3}$	$-1.04658 \cdot 10^{-3}$
0.04	-1	$-16.7097 \cdot 10^{-3}$	$-16.0447 \cdot 10^{-3}$
0.04	1	$-10.1009 \cdot 10^{-3}$	$-10.1116 \cdot 10^{-3}$
0.4	-1	$-15.2877 \cdot 10^{-3}$	$-15.3012 \cdot 10^{-3}$

**Table 8**  
Parallel bearings characteristics in Ref. [27].

Bearing length:	20 mm
Bearing width:	20 mm
Clearance:	$h_0 = 4\mu\text{m}$
Velocity:	10 m/s
Viscosity:	$\eta = 10\text{mPa}\cdot\text{s}$
Ambient pressure:	100 kPa
Cavitation pressure:	90 kPa
Dimple radius:	$r = 500\mu\text{m}$
Dimple depth:	$a = 10\mu\text{m}$

**Table 9**  
Comparison with the Profito et al. results in Ref. [27].

Texture	[27] results	Present code results
10 × 10	38.91 N	38.95 N
10 × 8	41.57 N	41.50 N
10 × 6	44.84 N	44.61 N
10 × 4	47.06 N	46.71 N
10 × 2	48.24 N	47.81 N

## References

- Etsion I, Halperin G, Brizmer V, Kligerman Y. Experimental investigation of laser textured parallel thrust bearings". *Tribol Lett* 2004;17(2):295–300.
- Kligerman Y, Etsion I, Shinkarenko A. Improving tribological performance of piston rings by partial surface texturing". *Transactions of the ASME. J Tribol* 2005;127:632–8.
- Brizmer V, Kligerman Y, Etsion I. A laser surface textured parallel thrust bearing". *Tribol Trans* 2003;46:397–403.
- Etsion I, Kligerman Y, Halperin G. Analytical and experimental investigation of laser-textured mechanical seal faces". *Tribol Trans* 1999;42(3):511–6.
- Ryk G, Kligerman Y, Etsion I. Experimental investigation of laser surface texturing for reciprocating automotive components". *Tribol Trans* 2002;45(4):444–9.
- Etsion I, Halperin G. A laser surface textured hydrostatic mechanical seal". *Tribol Trans* 2002;45(3):430–4.
- Tonder K. Hydrodynamics effects of tailored inlet roughness: extended theory". *Tribol Int* 2004;37:137–42. Elsevier.
- Vladescu SC, Medina S, Olver AV, Pegg IG, Reddyhoff T. Lubricant film thickness and friction force measurements in a laser surface textured reciprocating line contact simulating the piston ring-liner pairing". *Tribol Int* 2016;98:317–9.
- Lu P, Wood RJK, Gee MG, Wang L, Pflieger W. The friction reducing effect of square-shaped surface textures under lubricated line-contacts - an experimental study". *Lubricants* 2016;4(3):26.
- Tomanik E. Modeling the hydrodynamic support of cylinder bore and piston rings with laser textured surfaces". *Tribol Int* 2013;59:90–6. Elsevier.
- Fowell MT, Olver AV, Gosman AD, Spikes HA, Pegg I. Entrainment and inlet suction: two mechanisms of hydrodynamic lubrication in textured bearings". *Transactions of the ASME. J Tribol* 2007;129:336–47.
- Fowell MT, Medina S, Olver AV, Spikes HA, Pegg IG. Parametric study of texturing in convergent bearings". *Tribology International* vol. 52. Elsevier; 2012. p. 7–16.
- Pascovici MD, Cicone T, Fillon M, Dobrica MB. Analytical investigation of a partially textured parallel slider". *Proc IME J J Eng Tribol* 2009;223(2):151–8.
- Rahmani R, Shirvani A, Shirvani H. Optimization of partially textured parallel thrust bearings with square-shaped micro-dimples". *Tribol Trans* 2007;50(3):401–6.
- Sahlin F, Glavatskih S, Almqvist T, Larsson R. Two-dimensional CFD-analysis of micro-patterned surfaces in hydrodynamic lubrication". *Transactions of the ASME. J Tribol* 2005;127:96–102.
- Menon Dileep P, Anil PM, Kulkarni Prakash S. An analysis on the influence of oil pocket shape and distribution on the reduction of friction in hydrodynamic lubrication". *17th Annual CFD Symposium*. 2015.
- Dobrica MB, Fillon M. About the validity of Reynolds equation and inertia effects in textured sliders of infinite width". *Proc IME J J Eng Tribol* 2009;223(1):69–78.
- Ausas R, Ragot P, Leiva J, Jai M, Bayada G, Buscaglia G. The impact of the cavitation model in the analysis of microtextured lubricated journal bearings". *Transactions of the ASME. J Tribol* 2007;129:868–75.
- Ausas R, Jai M, Ciuperca I, Buscaglia G. Conservative one-dimensional finite volume discretization of a new cavitation model for piston-ring lubrication". *Tribol Int* 2013;57:54–66. Elsevier.
- Qiu Y, Khonsari MM. On the prediction of cavitation in Dimples using a mass-conservative algorithm". *Transactions of the ASME. J Tribol* 2009;131. 041702-1–041702-11.
- Vijayaraghavan D, Keith Jr. TG. Development and evaluation of a cavitation algorithm". *Tribol Trans* 1989;32(2):225–33.
- Bayada G, Martin S, Vasquez C. An average flow model of the Reynolds roughness including a mass-flow preserving cavitation model. , *Transactions of the ASME, Journal of tribology* 2005;127:793–802.
- Giacopini M, Fowell MT, Dini D, Strozzi A. A mass-conserving complementarity formulation to study lubricant films in the presence of cavitation". *Transactions of the ASME. J Tribol* 2010;132. 041702-1–041702-12.
- Bertocchi L, Dini D, Giacopini M, Fowell MT, Baldini A. Fluid film lubrication in the presence of cavitation: a mass-conserving two-dimensional formulation for compressible, piezoviscous and non-Newtonian fluids". *Tribol Int* 2013;67:61–71. Elsevier.
- Elrod HG, Adams ML. A computer program for cavitation and starvation problems". *Proceedings of the 1st Leeds-Lyon symposium on tribology*. 1974. p. 37–41.
- Elrod HG. A cavitation algorithm". *ASME J. of Lub. Tech* 1981:350–4.
- Profito FJ, Giacopini M, Zachariadis DC, Dini D. A general finite volume method for the solution of the Reynolds lubrication equation with a mass-conserving cavitation model". *Tribol Lett* 2015;60.
- Woloszynski T, Podsiadlo P, Stachowiak GW. Efficient solution to the cavitation problem in hydrodynamic lubrication". *Tribol Lett* 2015;58(1). Springer.
- Biboulet N, Lubrecht AA. Efficient solver implementation for Reynolds equation with mass-conserving cavitation". *Tribol Int* 2018;118:295–300.
- Dobrica MB, Fillon M, Pascovici MD, Cicone T. Optimizing surface texture for hydrodynamic lubricated contacts using a mass-conserving numerical approach". *Proc IME J J Eng Tribol* 2010;224:737–50.
- Cupillard S, Glavatskih S, Cervantes MJ. Computational fluid dynamic analysis of a journal bearing with surface texturing". *Proc IME J J Eng Tribol* 2007;222(4):97–107.
- Cupillard S, Cervantes MJ, Glavatskih S. Pressure buildup mechanism in a textured inlet of a hydrodynamic contact". *Transactions of the ASME, Journal of tribology* 2008;130(4). 021701-1–021701-10.
- Tala-Ighil N, Fillon M, Maspeyrot P. Effect of textured area on the performances of a hydrodynamic journal bearing". *Tribol Int* 2011;44(3):211–9. Elsevier.
- Shen C, Khonsari MM. On the magnitude of cavitation pressure of steady-state lubrication". *Tribol Lett* 2013;51:153–60.
- Shen C, Khonsari MM. Effect of dimple's internal structure on hydrodynamic lubrication". *Tribol Lett* 2013;52:415–30.
- Shen C, Khonsari MM. Numerical optimization of texture shape for parallel surfaces under unidirectional and bidirectional sliding". *Tribol Int* 2015;82:1–11. Elsevier.
- Shen C, Khonsari MM. The effect of laser machined pockets on the lubrication of piston ring prototypes". *Tribology international* vol. 101. Elsevier; 2016. p. 273–83.
- Gherca AR, Maspeyrot P, Hajjam M, Fatu A. Influence of texture geometry on the hydrodynamic performances of parallel bearings". *Tribol Trans* 2013;56(3):321–32.
- Gherca AR, Fatu A, Hajjam M, Maspeyrot P. Influence of surface geometry on the hydrodynamic performances of parallel bearings in transient flow condition". *Tribol Trans* 2013;56:953–67.
- Gherca A.R., Fatu A., Hajjam M., Maspeyrot P. "Effects of surface texturing in steady-state and transient flow conditions: two-dimensional numerical simulation using a mass-conserving cavitation model". *Proc IME J J Eng Tribol*, volume 229(4), p. 505–522.
- Alcouffe RE, Brandt A, Dendy JE, Painter JW. The multi-grid method for the diffusion equation with strongly discontinuous coefficients". *SIAM J Sci Stat Comput* 1981;2:430–54.
- Noutary M-P. A robust Reynolds solver for textured surfaces in the piston-ring cylinder liner contact INSA Lyon; 2017. PhD Thesis.
- Brandt A. 1984 multigrid guide, lightly revised 2011". 2011http://www.wisdom.weizmann.ac.il/achi/.
- Venner CH, Lubrecht AA. Multilevel methods in lubrication" vol. 37. *Tribology Series*: Elsevier; 2000.
- Ryk G, Etsion I. Testing piston rings with partial laser surface texturing for friction reduction" vol. 261. *Wear*: Elsevier; 2006. p. 792–6.
- Etsion I, Sher E. Improving fuel efficiency with laser surface textured piston rings". *Tribol Int* 2009;42:542–7.